

# Quantitative Analysis of Transcranial and Intraparenchymal Light Penetration in Human Cadaver Brain Tissue

Clark E. Tedford,<sup>1</sup> Scott DeLapp,<sup>1</sup> Steven Jacques,<sup>2</sup> and Juanita Anders<sup>3\*</sup>

<sup>1</sup>*LumiThera, Inc., Poulsbo, Washington 98370*

<sup>2</sup>*Oregon Health and Science University, Portland, Oregon*

<sup>3</sup>*Department of Anatomy, Physiology and Genetics, Uniformed Services University of the Health Sciences, Bethesda, Maryland 20814*

**Background and Objective:** Photobiomodulation (PBM) also known as low-level light therapy has been used successfully for the treatment of injury and disease of the nervous system. The use of PBM to treat injury and diseases of the brain requires an in-depth understanding of light propagation through tissues including scalp, skull, meninges, and brain. This study investigated the light penetration gradients in the human cadaver brain using a Transcranial Laser System with a 30 mm diameter beam of 808 nm wavelength light. In addition, the wavelength-dependence of light scatter and absorbance in intraparenchymal brain tissue using 660, 808, and 940 nm wavelengths was investigated.

**Study Design/Material and Methods:** Intact human cadaver heads ( $n = 8$ ) were obtained for measurement of light propagation through the scalp/skull/meninges and into brain tissue. The cadaver heads were sectioned in either the transverse or mid-sagittal. The sectioned head was mounted into a cranial fixture with an 808 nm wavelength laser system illuminating the head from beneath with either pulsed-wave (PW) or continuous-wave (CW) laser light. A linear array of nine isotropic optical fibers on a 5 mm pitch was inserted into the brain tissue along the optical axis of the beam. Light collected from each fiber was delivered to a multichannel power meter. As the array was lowered into the tissue, the power from each probe was recorded at 5 mm increments until the inner aspect of the dura mater was reached. Intraparenchymal light penetration measurements were made by delivering a series of wavelengths (660, 808, and 940 nm) through a separate optical fiber within the array, which was offset from the array line by 5 mm. Local light penetration was determined and compared across the selected wavelengths.

**Results:** Unfixed cadaver brains provide good anatomical localization and reliable measurements of light scatter and penetration in the CNS tissues. Transcranial application of 808 nm wavelength light penetrated the scalp, skull, meninges, and brain to a depth of approximately 40 mm with an effective attenuation coefficient for the system of  $2.22\text{ cm}^{-1}$ . No differences were observed in the results between the PW and CW laser light. The intraparenchymal

studies demonstrated less absorption and scattering for the 808 nm wavelength light compared to the 660 or 940 nm wavelengths.

**Conclusions:** Transcranial light measurements of unfixed human cadaver brains allowed for determinations of light penetration variables. While unfixed human cadaver studies do not reflect all the conditions seen in the living condition, comparisons of light scatter and penetration and estimates of fluence levels can be used to establish further clinical dosing. The 808 nm wavelength light demonstrated superior CNS tissue penetration. *Lasers Surg. Med.*

© 2015 Wiley Periodicals, Inc.

**Key words:** central nervous system; isotropic optical fibers; low level light therapy; photobiomodulation; transcranial light therapy; 808 nm wavelength

## INTRODUCTION

Photobiomodulation (PBM), also referred to as low-level light therapy, uses non-thermal red and near infrared light (600–1000 nm) to alter cellular and tissue function by the interaction of photons with one or more chromophores [1,2]. Recent reviews summarized the data supporting the mechanisms that underlie PBM [3,4] including the absorption of near-infrared (NIR) light by the terminal enzyme in the mitochondrial respiratory chain, cytochrome C oxidase. The energy absorbed by cytochrome C oxidase leads to increased enzyme activity and production of ATP. Critical downstream signaling cascades are also activated [5–7]. NIR light causes increased ATP and reactive oxygen species production, nitric oxide release,

Contract grant sponsor: CRADA between USUHS and Photothera, Inc.; Contract grant number: # G1709V.

\*Correspondence to: Juanita J. Anders, PhD, Department of Anatomy, Physiology and Genetics, Uniformed Services University of the Health Sciences, 4301 Jones Bridge Road, Bethesda, MD 20814. E-mail: [juanita.anders@usuhs.edu](mailto:juanita.anders@usuhs.edu)

Accepted 5 January 2015

Published online in Wiley Online Library

([wileyonlinelibrary.com](http://wileyonlinelibrary.com)).

DOI 10.1002/lsm.22343

and cyclic AMP production, all of which can contribute to beneficial effects in tissues with compromised function [4]. *In vitro* and *in vivo* studies have shown that PBM can directly modify markers of inflammation and oxidative stress [8–12], reduce pain [13], and prevent cell death [7,14] in a number of tissue types. More recently, a growing number of preclinical and clinical published reports have shown positive outcomes for PBM in diseases and injuries related to the central nervous system (CNS) [11,15–29].

Non-invasive delivery of photons from the light source to the brain for the treatment of brain injuries and diseases is termed transcranial light therapy (TLT). TLT holds promise as a treatment for acute conditions including ischemic stroke and traumatic brain injury (TBI), as well as global ischemia following cardiac arrest. It also has the potential to improve cellular function in age-related neurodegenerative CNS diseases that include Alzheimer's Disease, Parkinson's Disease, and Huntington's Disease and to restore normal metabolic activity in psychiatric illnesses including Major Depressive Disorders.

We recently analyzed transcranial light penetration in anesthetized rats, mice, and rabbits. In these animals, a single NIR light application site on the scalp irradiated the entire brain. Positive effects of TLT have been reported in animal models of acute TBI [15–17], Alzheimer's Disease [20], depression [18], and cerebral ischemia [24–28]. In humans, TLT improved cognition in two chronic TBI cases [19] and increased regional cerebral blood flow and improved the psychological status of patients with depression [23]. No adverse side effects were noted in these studies. In fact, safety of TLT for human use was demonstrated in a clinical trial for treatment of ischemic stroke [29,30]. Based on the preclinical work and cadaver measurements done to support the ischemic stroke clinic trial, it was determined that delivery of energy density of 7–10 mW/cm<sup>2</sup> was an effective dose for photobiomodulation of the injured cortex (personal communication and [31]).

The expansion of PBM as an effective, non-invasive, and innovative non-pharmaceutical approach to treat human brain injuries and diseases requires an in-depth understanding of light propagation through the scalp, skull, meninges, and brain. Human cadaver studies provide one approach to determine optimal light treatment parameters to target global or specific brain structures. Human scalp, skull, and brain tissue have been examined for absorption and scattering properties of light [32] and for NIR light transmission and attenuation [33] *in vivo* during brain surgery. Transmittance and diffuse reflectance of *ex vivo* samples of human cadaver skull [34] and skull and scalp and brain have also been measured [35–37].

The objective of this study was to characterize the transmission of 808 nm wavelength light through non-fixed, intact human scalp, skull, meninges, and brain at various depths and locations. Additionally, the attenuation through the intraparenchymal brain tissue was characterized locally at wavelengths of 660, 808, and 940 nm.

## METHODS

### Cadaver Laser System

The Laser System was a research device specifically designed to provide non-invasive TLT to cadavers (Fig. 1). The instrument provided high power capacity and a temperature controlled primary laser affixed to a stereotactic apparatus. The system included a Primary Laser and three Reference Lasers of different wavelengths. The basic characteristics of these lasers are presented in Table 1.

The Laser System consisted of a console (location of control electronics), a laptop computer, a primary laser assembly (location of the laser source and interface to the cadaver tissue), a reference laser system with three wavelengths for brain parenchyma measurements, a power verification unit, a cart assembly, a cranial fixture, and data collection equipment. The treatment modality was a predetermined sequence that was preprogrammed into the Research Device Console and data acquisition was controlled and stored by a laptop computer. A treatment regimen consisted of either treating a user-determined location on the cadaver scalp with the primary laser or treating locally in the brain with the reference laser probes. The Primary Laser Research Device utilized a laser diode source and had a maximal output power of 50 W continuous wave (CW) or 70 W pulsed wave (PW) at a wavelength of 808 nm and nominal beam diameter of 30 mm applied to the surface of the head of cadavers. CW and PW were examined to determine if pulsing altered fluence rate.

### Power Measurements

Measurement of the optical power within the tissue was accomplished by sampling the light with an array of nine 400  $\mu$ m fibers each with an isotropic detector (Medlight IP85). Each fiber was bonded into a stainless steel hypodermic tubing at the collection end to provide mechanical rigidity (Fig. 2). The isotropic probes were

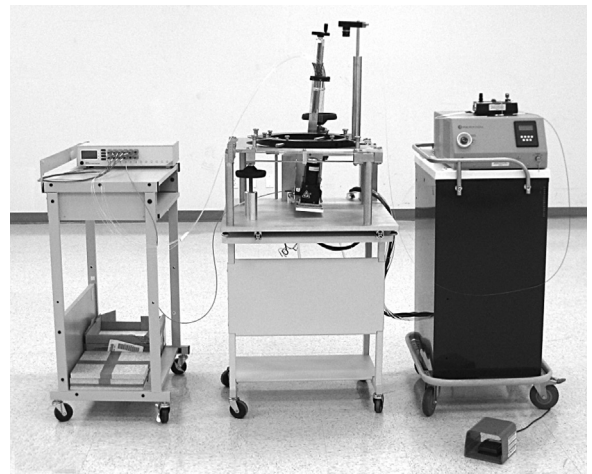


Fig. 1. Photograph of the cadaver laser system and the cranial fixture.

**TABLE 1. Laser System Overview: Basic Characteristics of the Primary and Three Reference Lasers**

Laser	808 nm Primary	660 nm Reference	808 nm Reference	940 nm Reference
Power supply	120V AC	3.5–5V DC	3.5–5V DC	3.5–5V DC
Emission power	70W max	50 mW max	50 mW max	50 mW max
Laser class	IV	IIIb	IIIb	IIIb
Laser diode	$4.6 \times 4.6$ VCSEL Array	Single mode diode	Single mode diode	Single mode diode
Beam type	Flat Top, <0.1 NA	Gaussian, 0.39 NA	Gaussian, 0.39 NA	Gaussian, 0.39 NA
Wavelength	$808 \pm 5$ nm	$660 \pm 3$ nm	$808 \pm 3$ nm	$940 \pm 6$ nm

used with a distance of 5 mm between the probes. Each fiber was connected to a separate channel of a multi-channel power meter (OptoTest OP710-Si), which was capable of a dynamic measurement range of +6 decibel-milliwatts (dBm) (4.0 mW) to  $-80$  dBm ( $1.0 \times 10^{-8}$  mW). An additional 1,000  $\mu\text{m}$  core optical fiber was run from another channel of the power meter to a sampling port within the laser assembly for continuous monitoring of laser output power. The total output power of the primary laser was measured with a thermal-based power detector (Ophir LD40–150) and meter (Ophir Nova), which contained a large enough collection area to capture the full 30 mm primary beam. Power from the emitting probes was measured using a single channel optical power and wavelength detector (ILX Lightwave OHM-6722B) connected to its associated meter (ILX Lightwave OMM-6810B). Characterization of the primary laser output in pulsed mode was performed using an amplified photodiode (Thorlabs PDA10A) and an oscilloscope (Tectronics TDS2024B).

### Instrument Calibration

Due to the multitude of sensors used to measure optical power in the study (i.e., 12 channels in the OP710, the ILX system, and the Ophir meter and detector), calibration of all the detectors to a single standard was required to reduce measurement error. The chosen standard was the ILX, which was NIST traceable. The calibration of the OP710 and associated collection fibers to the ILX was undertaken by a lengthy procedure that involved the following abbreviated steps: (1) the probes and power meter channels were serialized such that a given probe would always be connected/reconnected to the same channel; (2) a spatially uniform beam (<2.5% variation) of 808 nm wavelength laser light was generated, and the fluence rate within the beam was measured using the ILX; (3) the angular response of each probe-channel was measured at the same point within the beam. This process was repeated with the probe tips submerged in water; and (4) a calibration factor was calculated for each probe-channel pair. This

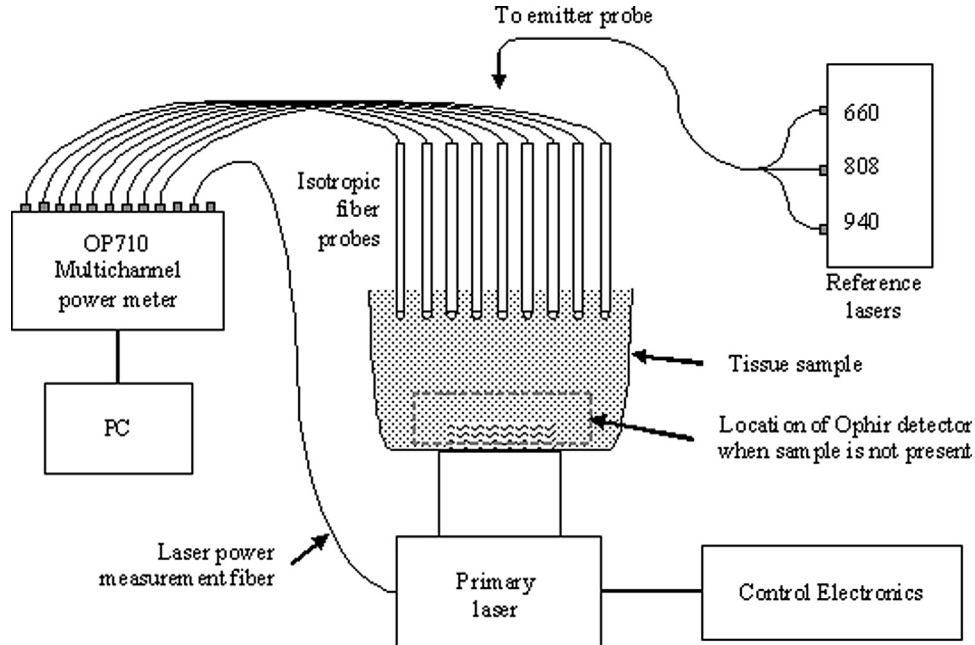


Fig. 2. Diagram of the cranial tissue fixture including the optical sensor probe array and laser.

factor was used to convert the indicated power on the multichannel power meter ( $\mu\text{W}$ ) to the actual fluence rate at the probe tip ( $\text{mW}/\text{cm}^2$ ). The Ophir detector was calibrated directly to the ILX by exposing each to the same laser source and calculating a percentage offset between the two.

### Cadaver Tissue

Cadaver heads ( $n = 8$ ) were used with permission of the USUHS Anatomical Materials Review Committee after review and approval of the submitted protocol. The eight cadavers ranged in age between 66 and 97. Unfixed cadaver tissue was utilized and the average number of days postmortem was 25. The extended post-mortem period was required to allow blood testing for infectious disease. The cause of death was reviewed and no CNS diseases or pathologies were included in the cadaver selections. Standard refrigerated conditions at USUHS Anatomical Teaching Laboratories were used for maintaining cadaver specimens. The morphology of the brain was very good with recognizable gray and white matter and defined nuclei.

### Experimental Procedure

Multiple sites on each head were selected for light penetration analysis under different parameter sets and at multiple depths. A total of 20 different sites were examined across the eight heads. Four of the eight heads were sectioned transversely. These heads were sectioned just dorsal to the top of the ear resulting in the upper portion of the calvarium with its intact scalp, skull, meninges, and brain portion. The remaining four heads were sectioned in the mid-sagittal plane. At this level, the cut passed through the occipital, parietal, and frontal lobes of the cerebral cortices. A transfer plate was placed on the cut side of the head to allow inversion and mounting of the sectioned head into the removable fixation ring. The head was secured by four positional screws into a cranial fixation ring. Once secured, the head was inverted again wherein the cut surface of the brain was dorsal and the top of the skull and scalp were in the ventral position. The removable fixation ring was placed into position in the cranial fixture and secured with the primary laser positioned below (Fig. 3). In this position, the optical sensor probe array was lowered for entry into the brain tissue. The probe array was constrained to move along the optical axis of the laser. The coordinates were recorded and established the laser light illumination path through the head at a fixed location and angle. Once the coordinates were secure, the primary laser was raised until the output lens was flush with the scalp, applying a light pressure ( $\sim < 5$  lbs). The sensor probe array was lowered to the cut surface of the brain and distance from the lens surface was recorded. The sensor probe array was then lowered into the brain tissue at 5 mm increments until the inner aspect of the dura mater was reached. At each 5 mm increment, the fluence rate at each probe was recorded.

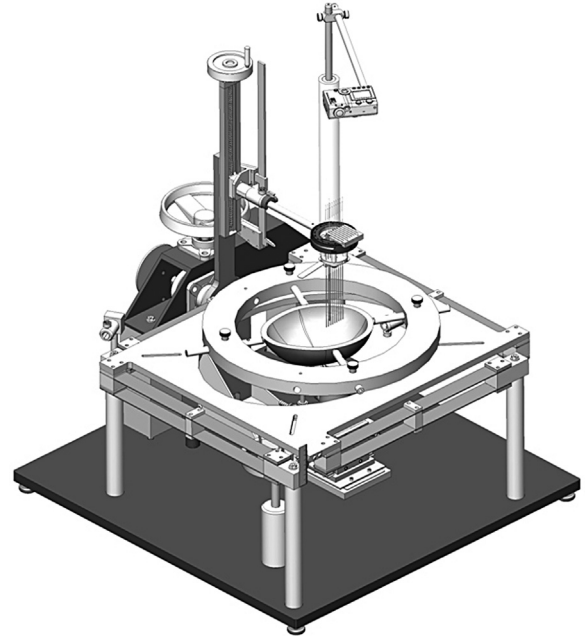


Fig. 3. Illustration of the cranial fixture with the optical sensor probe array (above) and laser delivery system (below).

Typically, a series of measurements was taken at each position within the tissue, corresponding to a different laser (primary laser 808 nm wavelength, reference lasers 660, 808, and 940 nm wavelengths) or modality (PW vs. CW). The general sequence at each depth was lower the probe array into the tissue and record probe depth; activate primary laser, 5 W CW and collect data; activate primary laser, pulsed at 10 Hz, 20% duty cycle (DC), 5 W peak power; collect data; activate primary laser, pulsed at 100 Hz, 20% DC, 5 W peak power; collect data; sequentially activate the reference lasers, 50 mW CW; collect data for each reference laser; lower the probe array 5 mm and repeat. This process was continued until the inner aspect of the dura mater was reached. A similar procedure was conducted for the mid-sagittal cuts. At each data collection, the collection time ranged from 2 to 6 seconds, with the power meter streaming all channels to the PC at a rate of 7 times per second. This resulted in 14–42 measurements of the fluence rate at each probe tip for every collection window.

### Data Analysis

The raw data collected from the multichannel power meter were converted to measured fluence rates using the previously calculated calibration factor for each probe. The data from each site were then normalized to an input laser power of 1 W on the surface of the scalp. For the primary laser, this normalization was performed on each acquisition using the power recorded from the laser power measurement fiber at the same instance, thus eliminating any potential errors due to laser power drifting over the course of sequential acquisitions. For the reference lasers,

normalization was performed using the reference laser powers measured at the start of each test. An additional correction to the data from the reference lasers was made to account for the wavelength-dependent sensitivity of the power meter. Raw data that fell below an established minimum detection level were discarded. The minimum detectable signal (also known as the noise floor) is the result of a number of factors including basic equipment responsiveness, electrical noise, stray light, fiber collection efficiency, etc. For this system, the level was established by taking a series of identical measurements sequentially throughout the tissue at 5 and at 15 W of primary laser power. Once normalized, the 5 and 15 W measurements would be expected to produce nearly identical results. Thus, the point at which these results begin to differ significantly can be taken as the point at which the noise begins to swamp the signal in the 5 W case. For this system, a percentage difference of <4% between the 5 and 15 W cases was selected as the threshold for minimum detectable signal. This difference was seen at approximately the 55–60 mm distance from the scalp. All raw data corresponding to values above this threshold were discarded. Because of the multiple anatomical brain substructures and unique set of angles of light penetration studied, comparative group data were generated but should be recognized as containing confounding variables. Confounding variables included subject variability, brain size, shape, age, which provided unique cadaver data sets and thus sample pooling is somewhat limited when group analysis was conducted.

## RESULTS

The measured fluence rate within the cadaver brain across the nine isotropic probes for a typical coronal section is presented in Fig. 4a. The external surface of the scalp, where the laser made contact, was defined to be the measurement origin. The maximal probe distance from the primary laser was the exposed surface of the dissected brain tissue, where the isotropic probes entered. All experiments were carried out in the dark to minimize noise caused by ambient light. This maximal probe distance varied from subject to subject depending on the level of the dissection. At the distance farthest away from the primary laser beam where the probes entered the tissue, typically depths of 60 mm or more, background minimal fluence rates were established. As the probes were lowered into the tissue and the distance to the internal cortical surface decreased, an increase in fluence rates was seen. This generally resulted in an exponential increase in the measured fluence rate for a given linear decrease in probe depth. The distance of the probe depth from the internal cortical surface to the external surface of the scalp was typically 5–15 mm. However, curvature of the skull and angle of the probe insertion impacted how close to the cortical surface each individual probe reached. A contour plot of the above data was generated to graphically illustrate the resultant light distribution within the tissue (Fig. 4b). Near the cortical surface, the center and adjacent probes showed the highest fluence rates, which generally

corresponds to the 30 mm beam diameter of the laser. Measurements taken beyond the lateral extent of the beam indicated lower fluence rates. Measurable power was observed at cortical depths of greater than 40 mm.

The data from all probes over all examined sites were collapsed into a single data set, and a curve of the form  $F(x) = F_0 e^{-ux}$  was fit using a least-squares method (Fig. 5a). The resulting value of  $u$  can be interpreted as the effective attenuation coefficient for the system, and was found to be  $2.22 \text{ cm}^{-1}$ . It is worth noting that a large driver of deviation in the data was the initial transmission through the scalp and the skull. Normalizing the data from each probe to  $1 \text{ mW/cm}^2$  at the inner surface of the skull removes the effect of the skull and scalp variability, and illustrates the optical variability in the brain tissue itself (Fig. 5b). The resting value of  $u$  was found to be  $2.43 \text{ cm}^{-1}$  when normalized.

The fluence rate was measured by a given probe with the primary laser operating sequentially in CW mode, pulsed at 10 Hz, 20% duty cycle, and pulsed at 100 Hz, 20% duty cycle. No difference was observed in the normalized fluence rates for any of the probes at any of the sites.

The results of the intraparenchymal brain tissue measurements using the internal emitter probe to launch reference laser wavelengths of 660, 808, and 940 nm directly into the brain tissue are presented in Figure 6. As with the data generated with the primary laser, any data beneath the established minimum detectable signal was discarded, and the results have been normalized to remove the power differences between each laser. The typical power emitted from each reference laser was  $\sim 40 \text{ mW}$ . There is clearly a higher attenuation of the 660 nm wavelength than the 940 nm wavelength and of the 940 nm wavelength compared to the 808 nm wavelength. In most instances, the 660 nm wavelength failed to produce a response in the outer two probes that was above the noise threshold.

The experimental values of  $\mu_{\text{eff}} [\text{cm}^{-1}]$  for cadaver brain at 660, 808, 940 nm wavelengths were compared to literature on brain tissues [38]. This comparison is shown in Figure 7. The experimental data are shown as  $\mu_{\text{eff}} [\text{cm}^{-1}]$  versus wavelength ( $\lambda$ ). Also shown is the least-squares fit to the data using diffusion theory, which specifies the blood volume fraction ( $B$ ), the hemoglobin oxygen saturation ( $S$ ), and the reduced scattering coefficient at 500 nm wavelength ( $\mu_s'_{500\text{nm}}$ ). Literature cited in Jacques, 2013 [38] provided spectra for comparison, and the median value of the scattering power ( $b$ ). The water content was assumed to be 0.75. The fitting was conducted on all the data at 660, 808, and 940 nm simultaneously, using the equation:

$$\mu_{\text{eff}} = \frac{1}{\sqrt{3\mu_a(\mu_a + \mu_s')}} \quad (1)$$

where

$$\mu_a = BS\mu_{a,\text{oxy}}(\lambda) + B(1-S)\mu_{a,\text{deoxy}}(\lambda) + W\mu_{a,\text{water}}(\lambda)$$

$$b = 1.41 \text{ (median of literature values for brain tissues)}$$

$$\mu_s' = \mu_s'_{500\text{nm}} (\lambda/500 \text{ nm})^{-b}$$

$$D = 1/(3(\mu_a + \mu_s'))$$

$$\mu_{\text{eff}} = \text{sqrt}(\mu_a/D)$$

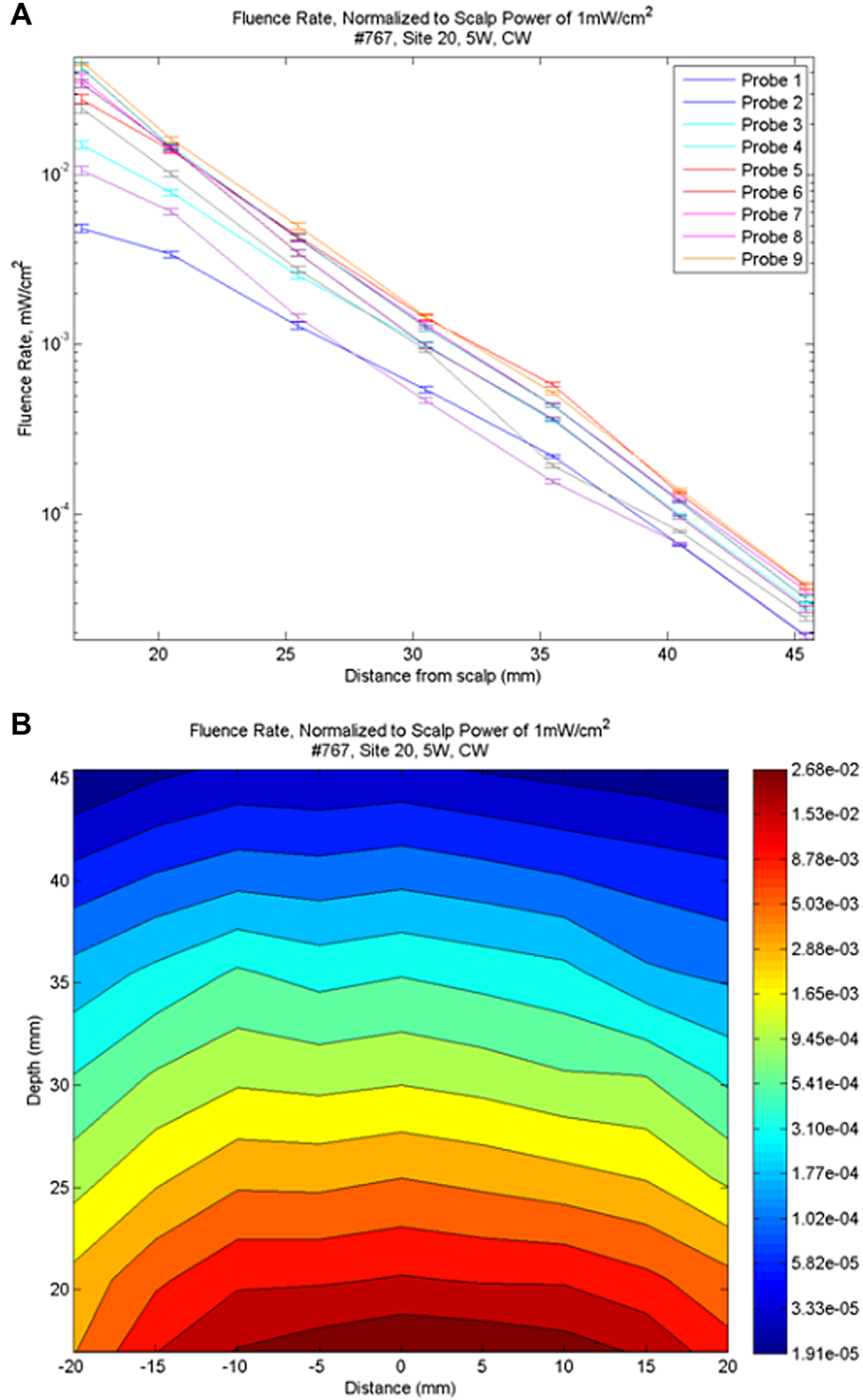


Fig. 4. NIR light fluence measurements in the human brain for a typical coronal section. (a) depicts the measured fluence rate at each of the nine individual isotropic detector probes. Measurements were serially collected at 5 mm depth of CNS tissue. Each data point represents a mean of data collected over several seconds while the primary laser was activated and the light intensity data was collected at a rate of 7 points/seconds. The data were normalized to 1 W at the external surface of the scalp. The fluence rates are provided in  $\text{mW}/\text{cm}^2$ . (b) depicts the same dataset as (a), plotted as a logarithmic contour plot to illustrate the spatial distribution of the fluence rate within the tissue.

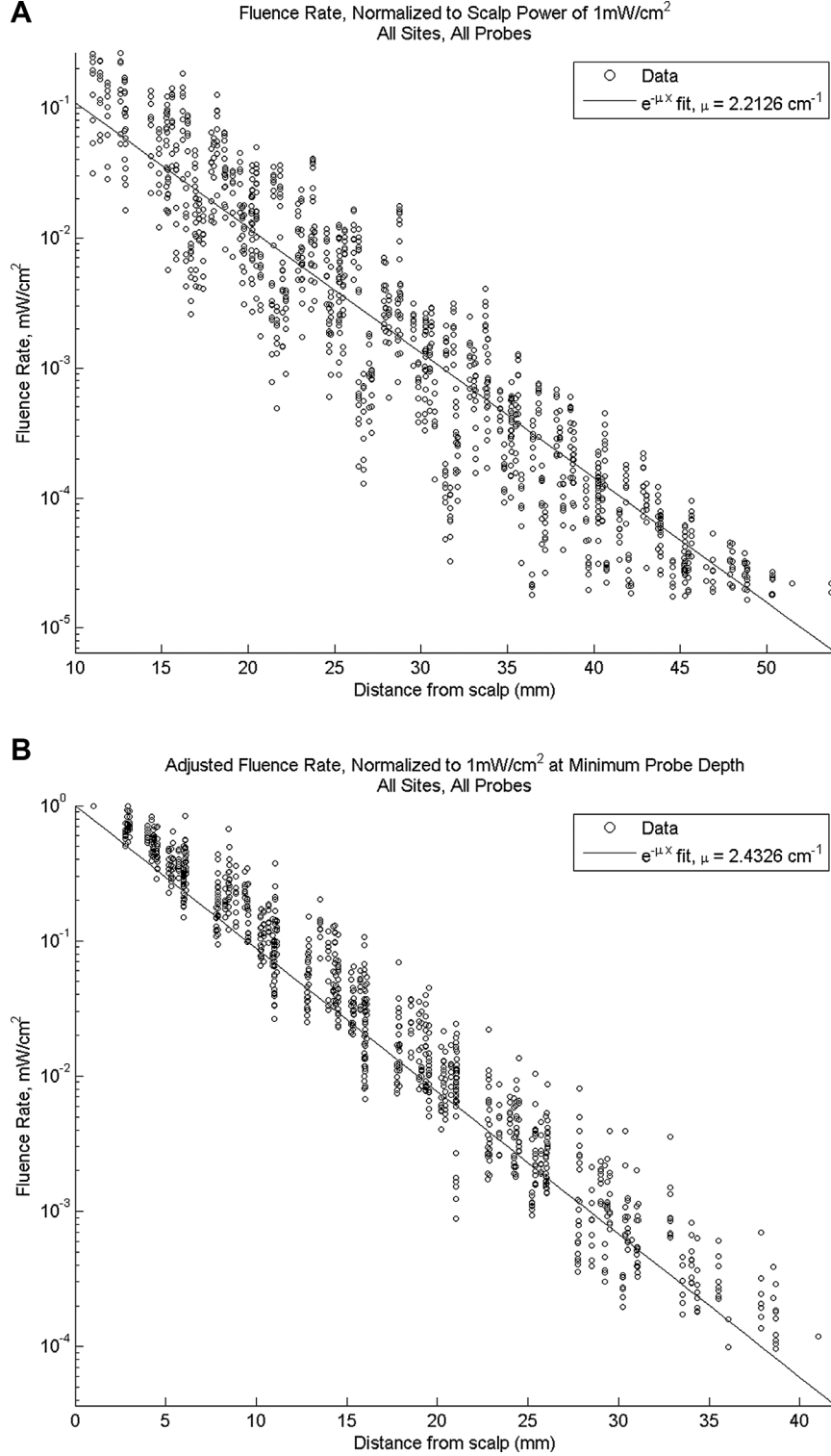


Fig. 5. (a) shows a composite plot of the fluence rates measured by all probes at all 20 sites examined (eight independent cadavers, various coronal, and sagittal dissections). Data below the established noise floor were discarded, and data from each site were normalized at each site to 1 W delivered to the surface of the scalp. The fluence rates are provided in  $\text{mW/cm}^2$ . A curve of the form  $F(x) = F_0 e^{-\mu x}$  was fit to the data using a least-squares method. (b) represents the same dataset, normalized at each site to 1 W at the cortical surface, rather than at the surface of the scalp. This removes the variability of the transmission through the scalp and skull and illustrates the variability in just the brain tissue.

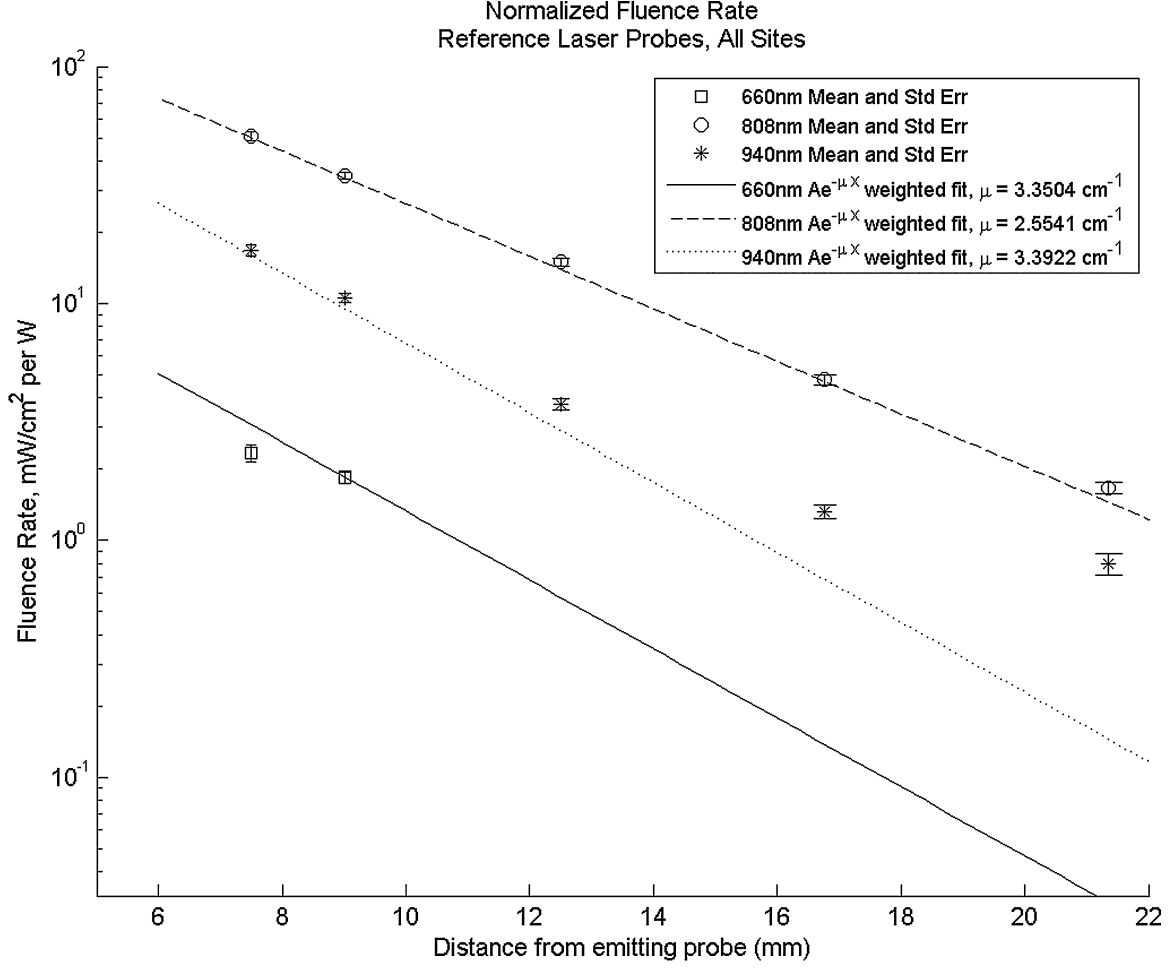


Fig. 6. Results of the intraparenchymal CNS fluence rate measurements at 660, 808, and 940 nm wavelengths for all probes at all sites examined. Data were normalized to 1 W from the emitter probe. The fluence rates are provided in mW/cm<sup>2</sup>.

and

$\mu_{a, \text{oxy}}(\lambda)$  is the absorption coefficient of oxygenated whole blood

$\mu_{a, \text{deoxy}}(\lambda)$  is the absorption coefficient of deoxygenated blood (whole blood defined as having 150 g hemoglobin/liter)

$\mu_{a, \text{water}}(\lambda)$  is the absorption coefficient of water.

Table 2 lists the optical properties,  $\mu_a$  and  $\mu_s'$ , of the cadaver brain for the three wavelengths.

## DISCUSSION

A critical component for establishing PBM as an effective therapy in CNS disorders is identifying and delivering the appropriate dose to alter aberrant cellular functions. While *in vitro* cellular and *in vivo* animal studies can provide clues to what light parameters and fluence rates are beneficial, scaling to the human condition is qualitative. Several animal studies have suggested the potential use of PBM in acute TBI [15–17], Alzheimer's Disease [20], depression [18], and cerebral ischemia [24–28]. In humans, TLT improved cognition in two chronic TBI cases [19] and increased regional cerebral blood flow and improved the psychological status of patients with depression [23].

The need to reach deep brain structures in many of these diseases and disorders is critical for establishing efficacy in long and costly human clinical trials. Recent failures in the use of TLT in stroke trials (Personal communication, Clark Tedford) may reflect the absence of consideration of the dosing parameters of NIR wavelengths in complex diseases or conditions. In this study, determination of transmission of 808 nm wavelength light through non-fixed, intact human scalp, skull, meninges, and brain at various depths and locations was undertaken to establish light penetration maps. These maps will help researchers and clinicians to better understand the potential dosing parameters required to provide an effective non-invasive treatment for CNS disorders. In addition, the absorption and scattering properties of the intraparenchymal brain tissue at wavelengths of 660, 808, and 940 nm were established to further aid in optimizing PBM parameters.

Human scalp, skull, and brain tissue have been examined for absorption and scattering properties of light [32] and for NIR light transmission and attenuation [33] *in vivo* during brain surgery. Transmittance and diffuse reflectance of *ex vivo* samples of human cadaver



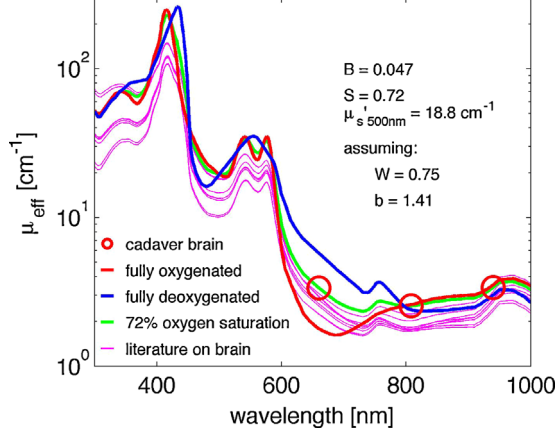


Fig. 7. Comparison of experimental values of  $\mu_{\text{eff}}$  [ $\text{cm}^{-1}$ ] for cadaver brain at 660, 808, 940 nm wavelengths (red circles), versus literature on brain tissues (magenta lines, cited in review by Jacques 2013 [38]). The diffusion theory fit to the cadaver brain data is shown as green line, with fitting parameters listed in figure. The diffusion theory predictions of fully oxygenated (red line) and fully deoxygenated (blue line) blood are shown.

skull [34] and skull, scalp and brain have also been measured [35–37]. Those studies involved transmission, scattering, and temperature measurements on excised non-preserved human skull and brain tissue as well as formalin preserved tissue. A number of these papers were referenced in a recent review of optical properties of biological tissues which compared the wavelength-dependent behavior of scattering and absorption of brain tissue to other tissues in the body [38].

Several limitations to the current study were identified during the course of data collection. The most obvious is the use of cadaver tissue, which may not mimic *in vivo* conditions. However, the instrument and detector probe capabilities were initially tested in fresh bovine brain and light scatter and penetration parameters were similar to those measured in the cadaver brains (unpublished observations). The non-fixed cadavers were kept refrigerated and the skulls were cut on the testing day immediately prior to evaluation. The anatomical landmarks and overall integrity of the CNS tissue was very good. The laser system was capable of collecting extensive and detailed information and was only limited by anatomical considerations. The laser beam was fixed in line with the array probe, which meant that the laser position and probe angle of entry was dependent on the size and shape of the skull. The study attempted to evaluate the same number of placements around the skull, but maintaining a flat laser contact with the scalp and skull

was the most critical and variable aspect which limited the ability to definitively collect same site data from subject to subject. This observation implies that a flexible apparatus would be most useful in the clinical instrument setting to allow for specific regional targeting.

Our results clearly demonstrate the penetration of measurable 808 nm wavelength light through the scalp, skull, and meninges to a brain depth of 40–50 mm. These data were used to create color-coded fluence maps of the NIR light as it penetrated the brain and scattered thus establishing a gradient of light energy as the photons were absorbed and distributed within the brain tissue. It is essential to understand these light fluence gradients within the brain to adjust the dose of light to reach the target tissues and provide a therapeutic range for CNS applications

In a previous study, post-mortem, human brain tissue was manually cut at non-specified thicknesses to establish gross penetration values [36]. In this study, four different wavelengths were tested: 632.8, 657, 780, and 835 nm. The optical penetration depth reported for each wavelength was  $0.92 \pm 0.08$ ,  $1.38 \pm 0.13$ ,  $3.46 \pm 0.23$ , and  $2.52 \pm 0.19$  mm, respectively. In another recent study, preserved cadaver skulls and heads that had been previously dissected or sectioned were used to measure transcranial red and NIR light transmission [37]. The light source consisted of LEDs emitting at peak wavelengths of either 633 or 830 nm with output powers in the  $\text{mW}/\text{cm}^2$  range ( $33.3 \text{ mW}/\text{cm}^2$ ) for the 830 nm wavelength and  $67.5 \text{ mW}/\text{cm}^2$  for the 633 nm wavelength. The relative percentages of light penetration were determined for various skull regions. For the occipital region which consisted of skull and some intact brain tissue (approximately 10 mm thick), it was 11.7% for the 830 nm wavelength and 0.7% of the 633 nm wavelength. Although the optical penetration depths reported earlier [36] were much less than we measured in our system, our intraparenchymal comparisons of light penetration of 660, 808, and 940 nm wavelengths confirmed that the NIR wavelength of 808 nm was superior in brain tissue penetration. Scattering and absorption of light is wavelength dependent [38] and is reflected in our wavelength-dependent transcranial light penetration data. This conclusion is also supported theoretically by Monte Carlo simulations that predicted near infrared light propagation in realistic head models [39–42]. Recognition of this wavelength-dependent transcranial and intraparenchymal light penetration is very important in establishing the potential use of PBM to treat CNS disorders. It appears highly unlikely that certain wavelengths would provide the transcranial depth of penetration needed for use in treating brain tissue. Continued research is needed to establish the optimal parameters for treatment of specific CNS diseases or disorders. In spite of the early stage of research into PBM treatment of CNS disorders, there is good evidence that NIR wavelengths will penetrate the scalp and skull and provide an opportunity for a non-invasive treatment.

**TABLE 2. Optical Properties of Cadaver Brain**

$\lambda$ [nm]	$\mu_a$ [ $\text{cm}^{-1}$ ]	$\mu_s'$ [ $\text{cm}^{-1}$ ]	$\mu_{\text{eff}}$ [ $\text{cm}^{-1}$ ]
808	0.22	9.5	22.2
940	0.47	7.7	21.8
660	0.29	12.7	21.5

## ACKNOWLEDGMENTS

The opinions and assertions contained herein are the private ones of the authors and are not to be construed as official or reflecting the views of the Department of Defense or the Uniformed Services University of the Health Sciences. The authors thank Mr. Ronald Rivenburgh, Anatomical Curator, for his help and expertise in the maintenance and preparation of the cadaver specimens. We want to thank Stephen Fry and Andreas Rose for their work on the calibration of the optical probes.

## REFERENCES

- Hamblin MR, Demidova-Rice TN. Cellular chromophores and signaling in low level light therapy. *Proc SPIE* 2007;6428: 1–14.
- Tata DB, Waynant RW. Laser therapy: A review of its mechanism of action and potential medical applications. *Laser Photonics Rev* 2011;5(1):1–12.
- Hashmi JT, Huang YY, Osmani BZ, Sharma SK, Naeser MA, Hamblin MR. Role of low-level laser therapy in neuro-rehabilitation. *PM R* 2010;2(12 Suppl 2):S292–S305.
- Naeser MA, Hamblin MR. Potential for transcranial laser or LED therapy to treat stroke, traumatic brain injury, and neurodegenerative disease. *Photomed Laser Surg* 2011;29(7):443–446.
- Eells JT, Henry MM, Summerfelt P, Wong-Riley MT, Buchmann EV, Kane M, Whelan NT, Whelan HT. Therapeutic photobiomodulation for methanol-induced retinal toxicity. *Proc Natl Acad Sci USA* 2003;100(6):3439–3444.
- Hourelid NN, Sekhejane PR, Abrahamse H. Irradiation at 830nm stimulates nitric oxide production and inhibits pro-inflammatory cytokines in diabetic wounded fibroblast cells. *Lasers Surg Med* 2010;42(6):494–502.
- Yip KK, Lo SCL, Leung MCP, So KF, Tang CY, Poon DMY. The effect of low-energy laser irradiation on apoptotic factors following experimentally induced transient cerebral ischemia. *Neuroscience* 2011;190(0):301–306.
- Assis L, Moretti AI, Abrahao TB, Cury V, Souza HP, Hamblin MR, Parizotto NA. Low-level laser therapy (808 nm) S reduces F inflammatory response, oxidative stress in rat tibialis anterior muscle after cryolesion. *Lasers Surg Med* 2012;44(9):726–735.
- Novoselova EG, Glushkova OV, Cherenkov DA, Chudnovsky VM, Fesenko EE. Effects of low-power laser radiation on mice immunity. *Photodermatol Photoimmunol Photomed* 2006;22(1):33–38.
- Lopes-Martins RAB, Penna SC, Joensen J, Iversen VV, Bjordal JM. Low level laser therapy (LLLT) in inflammatory and rheumatic diseases: A review of therapeutic mechanisms. *Curr Rheumatol Rev* 2007;3(2):147–154.
- Byrnes KR, Waynant RW, Ilev IK, Wu X, Barna L, Smith K, Heckert R, Gerst H, Anders JJ. Light promotes regeneration and functional recovery and alters the immune response after spinal cord injury. *Lasers Surg Med* 2005;36(3):171–185.
- Alcántara CC, Gigo-Benato D, Salvini TF, Oliveira ALR, Anders JJ, Russo TL. Effect of low-level laser therapy (LLLT) on acute neural recovery and inflammation-related gene expression after crush injury in rat sciatic nerve. *Lasers Surg Med* 2013;45(4):246–252.
- Chow RT, Johnson MI, Lopes-Martins RAB, Bjordal JM. Efficacy of low-level laser therapy in the management of neck pain: A systematic review and meta-analysis of randomised placebo or active-treatment controlled trials. *Lancet* 2009;374(9705):1897–1908.
- Frigo L, Favero GM, Lima HJ, Maria DA, Bjordal JM, Joensen J, Iversen VV, Marcos RL, Parizzoto NA, Lopes-Martins RA. Low-level laser irradiation (InGaAlP-660 nm) S increases F fibroblast cell proliferation, reduces cell death in a dose-dependent manner. *Photomed Laser Surg* 2010;28(Suppl 1): S151–S156.
- Oron A, Oron U, Streeter J, de Taboada L, Alexandrovich A, Trembovler V, Shohami E. Low-level laser therapy applied transcranially to mice following traumatic brain injury significantly reduces long-term neurological deficits. *J Neurotrauma* 2007;24(4):651–656.
- Ando T, Xuan W, Xu T, Dai T, Sharma SK, Kharkwal GB, Huang YY, Wu Q, Whalen MJ, Sato S, Obara M, Hamblin MR. Comparison of therapeutic effects between pulsed and continuous wave 810-nm wavelength laser irradiation for traumatic brain injury in mice. *PLoS ONE* 2011;6(10):e26212.
- Wu Q, Xuan W, Ando T, Xu T, Huang L, Huang YY, Dai T, Dhital S, Sharma SK, Whalen MJ, Hamblin MR. Low-level laser therapy for closed-head traumatic brain injury in mice: Effect of different wavelengths. *Lasers Surg Med* 2012;44(3):218–226.
- Wu X, Alberico SL, Moges H, De Taboada L, Tedford CE, Anders JJ. Pulsed light irradiation improves behavioral outcome in a rat model of chronic mild stress. *Lasers Surg Med* 2012;44(3):227–232.
- Naeser MA, Saltmarche A, Krengel MH, Hamblin MR, Knight JA. Improved cognitive function after transcranial, light-emitting diode treatments in chronic, traumatic brain injury: Two case reports. *Photomed Laser Surg* 2011;29(5):351–358.
- De Taboada L, Yu J, El-Amouri S, Gattioni-Celli S, Richieri S, McCarthy T, Streeter J, Kindy MS. Transcranial laser therapy attenuates amyloid-beta peptide neuropathology in amyloid-beta protein precursor transgenic mice. *J Alzheimer's Dis* 2011;23(3):521–535.
- Trimmer P, Schwartz K, Borland MK, De Taboada L, Streeter J, Oron U. Reduced axonal transport in Parkinson's disease cybrid neurites is restored by light therapy. *Mol Neurodegeneration* 2009;4(1):26.
- Komel'kova LV, Vitreshchak TV, Zhirnova IG, Poleshchuk VV, Stvolinskii SL, Mikhailov VV, Gannushkina IV, Piradov MA. Biochemical and immunological induces of the blood in Parkinson's disease and their correction with the help of laser therapy. *Patol Fiziol Eksp Ter* 2004;(1):15–18.
- Schiffer F, Johnston AL, Ravichandran C, Polcari A, Teicher MH, Webb RH, Hamblin MR. Psychological benefits 2 and 4 weeks after a single treatment with near infrared light to the forehead: A pilot study of 10 patients with major depression and anxiety. *Behav Brain Funct* 2009;5:46.
- Oron A, Oron U, Chen J, Eilam A, Zhang C, Sadeh M, Lampl Y, Streeter J, DeTaboada L, Chopp M. Low-level laser therapy applied transcranially to rats after induction of stroke significantly reduces long-term neurological deficits. *Stroke* 2006;37(10):2620–2624.
- Detaboada L, Ilic S, Leichter-Martha S, Oron U, Oron A, Streeter J. Transcranial application of low-energy laser irradiation improves neurological deficits in rats following acute stroke. *Lasers Surg Med* 2006;38(1):70–73.
- Lapchak PA, Wei J, Zivin JA. Transcranial infrared laser therapy improves clinical rating scores after embolic strokes in rabbits. *Stroke* 2004;35(8):1985–1988.
- Lapchak PA, Salgado KF, Chao CH, Zivin JA. Transcranial near-infrared light therapy improves motor function following embolic strokes in rabbits: An extended therapeutic window study using continuous and pulse frequency delivery modes. *Neuroscience* 2007;148(4):907–914.
- Lapchak PA, De Taboada L. Transcranial near infrared laser treatment (NILT) increases cortical adenosine-5'-triphosphate (ATP) content following embolic strokes in rabbits. *Brain Res* 2010;1306:100–105.
- Lampl Y, Zivin JA, Fisher M, Lew R, Welin L, Dahlof B, Borenstein P, Andersson B, Perez J, Caparo C, Ilic S, Oron U. Infrared laser therapy for ischemic stroke: A new treatment strategy: Results of the NeuroThera Effectiveness and Safety Trial-1 (NEST-1). *Stroke* 2007;38(6):1843–1849.
- Zivin JA, Albers GW, Bornstein N, Chippendale T, Dahlof B, Devlin T, Fisher M, Hacke W, Holt W, Ilic S, Kasner S, Lew R, Nash M, Perez J, Rymer M, Schellinger P, Schneider D, Schwab S, Velkamp R, Walker M, Streeter J. Effectiveness and safety of transcranial laser therapy for acute ischemic stroke. *Stroke* 2009;40(4):1359–1364.
- McCarthy TJ, De Taboada L, Hildebrandt PK, Ziemer EL, Richieri SP, Streeter J. Long-term safety of single and multiple infrared transcranial laser treatments in Sprague-Dawley rats. *Photomed Laser Surg* 2010;28(5):663–667.

32. Bevilacqua F, Pigué D, Marquet P, Gross JD, Tromberg BJ, Depeursinge C. In vivo local determination of tissue optical properties: Applications to human brain. *Appl Opt* 1999;38(22):4939–4950.
33. Young AE, Germon TJ, Barnett NJ, Manara AR, Nelson RJ. Behaviour of near-infrared light in the adult human head: Implications for clinical near-infrared spectroscopy. *Br J Anaesth* 2000;84(1):38–42.
34. Bashkatov AN, Genina EA, Kochubey VI, Tuchin VV. Optical properties of human cranial bone in the spectral range from 800 to 2000 nm. *Proc SPIE* 2006; 6163:616310–616310–616311.
35. Lychagov VV, Tuchin VV, Vilensky MA, Reznik BN, Ichim T, De Taboada L. Experimental study of NIR transmittance of the human skull. 2006; p 60850T–60850T–60855.
36. Stolik S, Delgado JA, Pérez A, Anasagasti L. Measurement of the penetration depths of red and near infrared light in human “ex vivo” tissues. *J Photochem Photobiol B* 2000; 57(2–3):90–93.
37. Jagdeo JR, Adams LE, Brody NI, Siegel DM. Transcranial red and near infrared light transmission in a cadaveric model. *PLoS ONE* 2012;7(10):e47460.
38. Jacques SL. Optical properties of biological tissues: A review. *Phys Med Biol* 2013;58(11):R37–R61.
39. Fukui Y, Ajichi Y, Okada E. Monte Carlo prediction of near-infrared light propagation in realistic adult and neonatal head models. *Appl Opt* 2003;42(16):2881–2887.
40. Okada E, Delpy DT. Near-infrared light propagation in an adult head model. I. Modeling of low-level scattering in the cerebrospinal fluid layer. *Appl Opt* 2003;42(16):2906–2914.
41. Okada E, Delpy DT. Near-infrared light propagation in an adult head model. II. Effect of superficial tissue thickness on the sensitivity of the near-infrared spectroscopy signal. *Appl Opt* 2003;42(16):2915–2922.
42. Custo A, Wells WM, 3rd, Barnett AH, Hillman EM, Boas DA. Effective scattering coefficient of the cerebral spinal fluid in adult head models for diffuse optical imaging. *Appl Opt* 2006;45(19):4747–4755.